# Fault-Dike-Magma Interactions Inferred from Transcrustal Conical Structures under Akutan Volcano

Vera Schulte-Pelkum\*1,2 and Matthew M. Haney<sup>3</sup>

#### Abstract

Volcano monitoring and eruption forecasting require accurate characterization of transcrustal magmatic structures to place volcanic unrest in context within the system where it occurs. Structural imaging using local seismicity is limited to seismogenic depths. Here, we exploit arrivals in teleseismic receiver functions that change polarity with backazimuth to image two surfaces beneath Akutan volcano in the Aleutian arc. The two surfaces delineate an upper to midcrustal inverted conical volume that deepens and thickens away from the volcanic center, with thicknesses of 3-13 km. The top of the volume is at depths of 2-3 km below sea level at distances of ~5-15 km from the caldera center. The bottom is at depths of 7-15 km at the same distances, and the cone's thickness increases outward from ~5 to ~10 km. The signal is best fit by a volume with anisotropy with fast symmetry planes that dip outward from the center and downward increases in shear velocity at both interfaces. The upper boundary coincides with the top of Akutan's volcanotectonic (VT) seismogenic zone, with the VT seismicity exhibiting outward dipping planar features that match the anisotropic fast plane orientation within the volume. The bottom of the anisotropic volume is below the termination depth of the majority of the VT seismicity and is therefore likely associated with the brittle-ductile transition. Long-period (LP) events associated previously with magma movement are concentrated below the anisotropic VT volume. Because of the strong spatial association with VT seismicity, we interpret the volume as consisting of concentric outward dipping faults and dikes that align the seismogenic response to stress changes from magmatic processes. Our observations map this volume independent of the present-day seismicity distribution and thus provide a spatially more complete image of the magmatic system.

Cite this article as Schulte-Pelkum, V., and M. M. Haney (2024). Fault–Dike–Magma Interactions Inferred from Transcrustal Conical Structures under Akutan Volcano, *Seismol. Res. Lett.* XX, 1–11, doi: 10.1785/0220240119.

**Supplemental Material** 

# Introduction

Concepts of magmatic systems under arc volcanoes have shifted from a traditional view of conduits feeding a single magma chamber in the upper crust to more complex transcrustal systems with storage levels possible throughout the crust (Cashman *et al.*, 2017). Models proposed for eruption forecasting (White and McCausland, 2019) predict unrest in different parts of the magmatic system at different pre-eruptive stages. Mapping the magmatic system is therefore of prime importance for volcanic monitoring.

Tomographic imaging using local seismicity is limited to depths above the seismogenic zone (e.g., Koulakov *et al.*, 2021). Monitoring networks on island arc volcanoes (Power *et al.*, 2020) are geographically restricted in aperture, which restricts the depth of resolution in ambient noise surface wave studies to the upper crust (e.g., Miller *et al.*, 2020). Teleseismic arrivals sample the entire crust and have steep arrival angles

that traverse the volume beneath the edifice in narrow-aperture networks. Receiver function studies use these ray paths and thus offer an opportunity for transcrustal imaging using island networks. A recent upgrade of most seismic stations to three-component broadband instrumentation for monitoring networks in Alaska (Power et al., 2020) makes receiver function analysis possible. In previous work using receiver functions in the Aleutian arc, central low-velocity zones were inferred using Moho conversion arrival times (Janiszewski et al., 2020; Portner et al., 2020) and receiver function arrival polarity

<sup>1.</sup> Cooperative Institute for Research in Environmental Sciences, University of Colorado Boulder, Boulder, Colorado, U.S.A., https://orcid.org/0000-0002-6057-5637 (VS-P); 2. Department of Geological Sciences, University of Colorado Boulder, Boulder, Colorado, U.S.A.; 3. U.S. Geological Survey, Alaska Volcano Observatory, Anchorage, Alaska, U.S.A., https://orcid.org/0000-0003-3317-7884 (MMH)

<sup>\*</sup>Corresponding author: verasp@colorado.edu

<sup>©</sup> Seismological Society of America

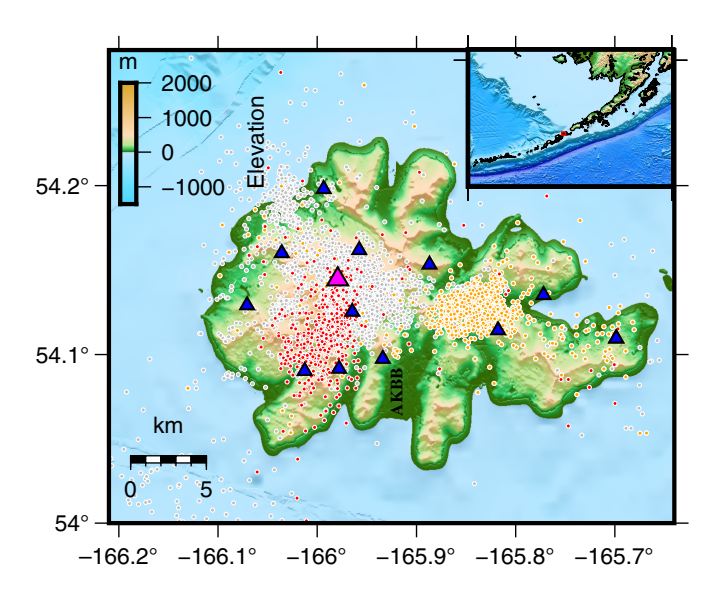


**Figure 1.** Map of Akutan volcano. The background color is elevation. The magenta triangle is the center of the summit caldera. Blue triangles are locations of seismic stations used for receiver function analysis; station AKBB featured in Figure 2 is marked. Gray dots are volcanotectonic (VT) seismicity event epicenters from the Alaska Volcano Observatory (AVO) catalog, with 1996 swarm in orange. The red dots are long-period (LP) events from the AVO catalog. The inset map shows the regional context, with the Bering Sea to the north, Alaska to the northeast, and subduction trench and Pacific plate to the south. Akutan Island is on the arc near the continental shelf break; the area on the main map is marked in red. The color version of this figure is available only in the electronic edition.

(Janiszewski et al., 2013). At Akutan, Janiszewski et al. (2013) noted receiver function arrivals that vary with backazimuth. Schulte-Pelkum, Caine, et al. (2020) inferred concentric structures at Alaskan volcanoes from receiver function polarity changes, attributed to anisotropy.

In the following, we examine the signal at Akutan volcano mentioned in Schulte-Pelkum, Caine, *et al.* (2020) in detail. Akutan is a basaltic–andesitic (Buurman *et al.*, 2014) stratovolcano in the center section of the long Aleutian arc over the subducting Pacific plate, near the transition from oceanic to continental overriding plate (Shillington *et al.*, 2004). As one of the most active volcanoes in the arc with 33 or more historical eruptions (see Data and Resources), it is classified as a "very high threat" (Ewert *et al.*, 2018). It has a Holocene caldera (Waythomas, 1999) on the western half of the island, with the rest of the island slightly elongated eastward from the volcano (Fig. 1).

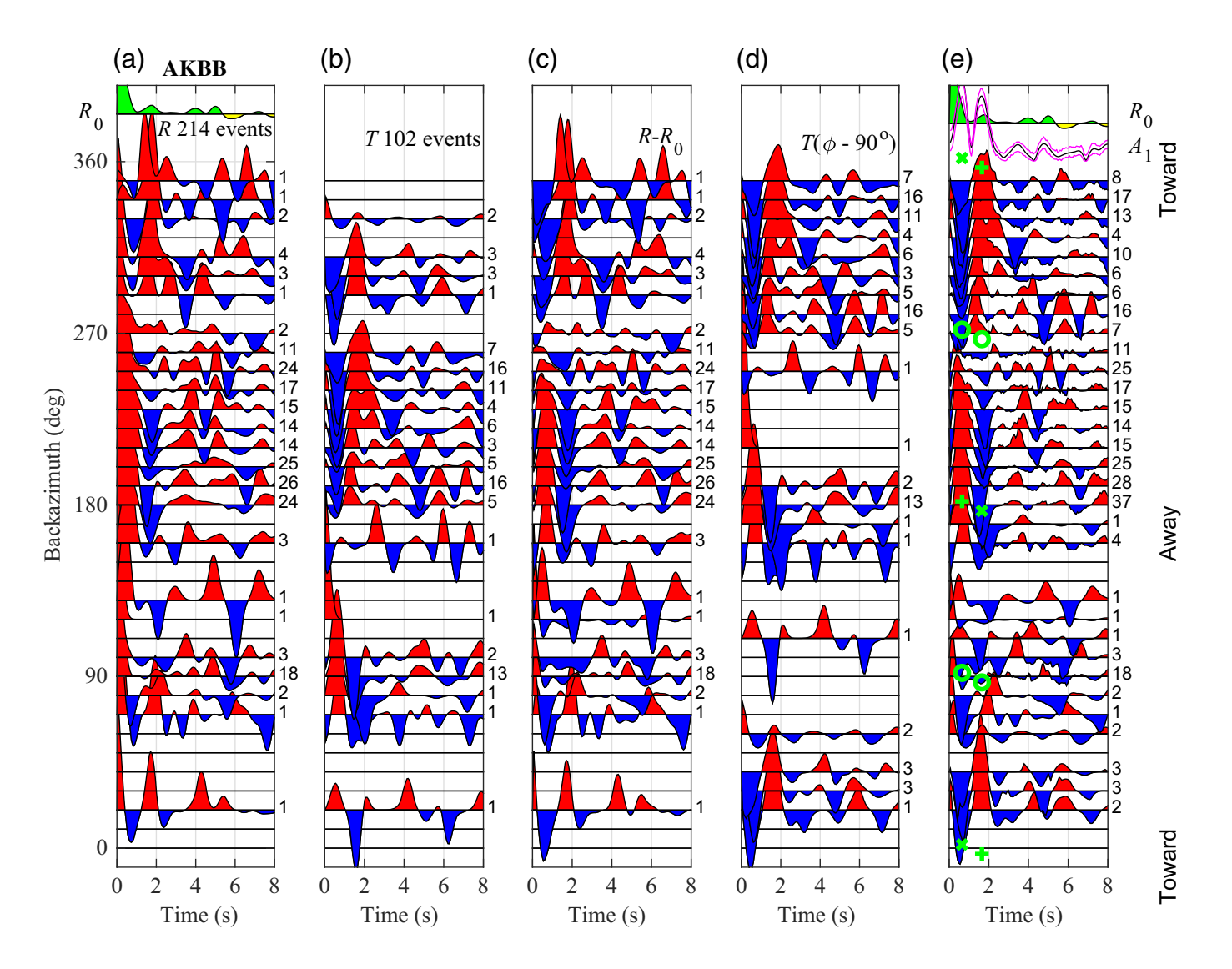
#### Method

We use stations (Fig. 1) of the Alaska Volcano Observatory (AVO) network (Power *et al.*, 2020) on Akutan Island with the addition of one station from the National Tsunami Warning Center Alaska Seismic Network, all for years 2015–2023. We

calculate iterative time domain radial and transverse component receiver functions (Ligorría and Ammon, 1999) for P and  $P_{\rm diff}$  arrivals of all teleseismic events at distances of 25°–150° with magnitude 5.0 or greater using a Gaussian filter factor of 3, corresponding to a pulse width of roughly 1 s. We apply an automated quality control and selection algorithm as described in Schulte-Pelkum and Mahan (2014b). Receiver functions at all stations exhibit very strong amplitude changes with backazimuth, including polarity flips, as observed previously in other studies (Janiszewski *et al.*, 2013).

Receiver functions record energy converted from P to S waves at interfaces beneath the station on the radial component, which represents particle motion in the earthquake-station plane (*P* to *SV* conversions). In the case of isotropic layers with horizontal interfaces, the amplitude of the conversion is independent of the station-to-earthquake backazimuth. When dipping interfaces or anisotropy are present, converted energy also appears on the transverse component perpendicular to the earthquake-station plane (P-SH scattering), and conversions on the radial component vary with backazimuth. We apply a method that isolates these conversions with out-of-plane particle motion and combines the signal from the radial and transverse components to obtain constraints on interface dip and plunging axis anisotropy (Schulte-Pelkum and Mahan, 2014a,b; Schulte-Pelkum, Ross, et al., 2020). A worked example for one of the Akutan stations is demonstrated in Figure 2. Figure 2a shows the radial component receiver functions used in standard analysis, here binned by backazimuth to balance uneven azimuthal sampling due to teleseismic event distributions. As described in previous work, receiver functions show a pronounced negative amplitude arrival at azimuths pointing toward the volcanic center (blue arrivals at less than 1 s delay time in Fig. 2a). There is a second arrival with polarity flips over backazimuth between 1 and 2 s delay time. Both arrivals are accompanied by large signals on the transverse component (Fig. 2b).

To isolate the azimuthally varying signal on the radial component, we subtract the azimuthal average radial receiver function  $R_0$  (average over all traces in Fig. 2a, shown at the top) from each trace in Figure 2a and obtain Figure 2c, which shows a strong 360° periodicity. Theoretical work (Park and Levin, 2016) and modeling (Schulte-Pelkum and Mahan, 2014a, b) show that in the case of hexagonally symmetric anisotropy with a plunging symmetry axis, the transverse component shows arrivals with a 360° periodicity that are offset 90° in backazimuth relative to those on the radial component. The same shift occurs in the presence of dipping interfaces in the isotropic case (Savage, 1998; Schulte-Pelkum and Mahan, 2014b). We therefore shift the transverse component traces in Figure 2b by 90° (equivalent to shifting the coordinate system by -90°) to obtain Figure 2d. A visual comparison shows the similarity between the radial traces corrected for  $R_0$  in Figure 2c and azimuth-shifted transverse traces in Figure 2d. We combine both sets of traces in Figure 2e to fill holes in backazimuthal

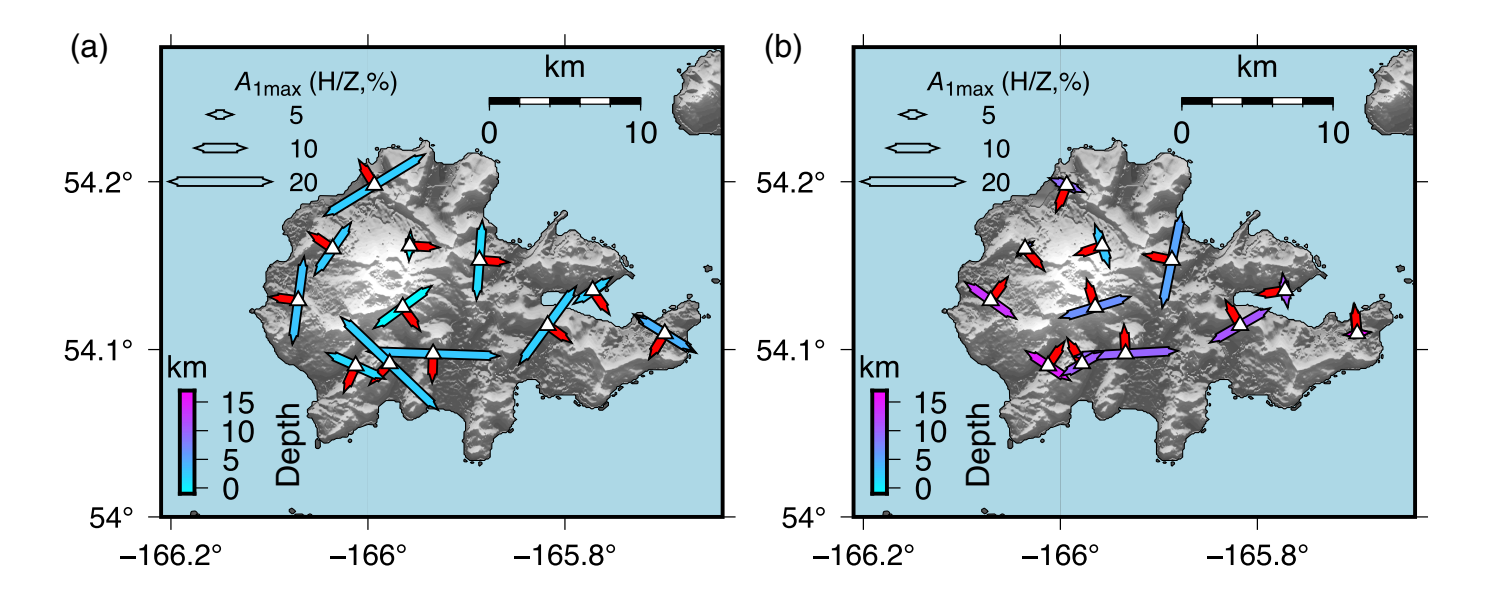


coverage. We then perform an azimuthal Fourier decomposition in a moving time window (Schulte-Pelkum and Mahan, 2014b) to solve for the amplitude  $A_1$  (Fig. 2e, top) and phase (Fig. 2e, green crosses) of the first azimuthal harmonic component. The phase points to the up- or downdip direction in the case of a dipping interface between isotropic layers and to the up- or downplunge direction of a symmetry axis in the case of a layer with plunging axis anisotropy. The azimuths perpendicular to the phase (where polarity flips occur) are parallel to the strike of a dipping interface or a dipping foliation. Both cases are detailed in Schulte-Pelkum, Ross, *et al.* (2020).

#### Results

Each receiver function arrival is generated at an interface with a contrast in material properties. The most commonly assumed geometry is a flat-layered medium with isotropic velocities. In this case, a positive polarity arrival seen on the radial component implies a shear velocity increase with depth at the interface, and a negative polarity arrival implies a shear velocity decrease with depth. A layer with low velocity would thus generate a negative polarity arrival from its top interface, followed

Figure 2. Analysis example for station AKBB south of Akutan volcano, location indicated in Figure 1. (a) Radial component receiver functions corrected for slowness and binned by backazimuth. Red represents positive and blue represents negative polarity. The small number on the right shows the number of traces per bin. No amplitude normalization is used. The top green (positive) and yellow (negative) trace is the azimuthal average of all binned traces,  $R_0$ . (b) Same as panel (a), but transverse component receiver functions. (c) Traces from panel (a) after subtracting  $R_0$  from each. (d) Traces from panel (b) after shifting by 90° in backazimuth to match predicted azimuthal behavior. (e) Traces in panels (c) and (d) combined. "Toward" and "away" mark azimuths pointing toward and away from the volcanic center, respectively. Blue trace with magenta error ranges  $A_1$  is the amplitude of the first azimuthal harmonic obtained from azimuthal Fourier analysis in a sliding time window. A pronounced  $A_1$  peak at 0.65 s (6.0 km depth below sea level) shows an amplitude maximum pointing away from the volcanic center (green cross) and a minimum toward the center (green x), with polarity flips tangential to the center (nodes marked by green circles). A second peak at 1.65 s (9.8 km depth) shows reversed maximum and minimum azimuths. The color version of this figure is available only in the electronic edition.



by a positive polarity arrival from its bottom interface. These arrivals should be identical at all backazimuths on the radial component, with no accompanying arrivals on the transverse component.

At azimuths pointing toward the volcano, Figure 2a,e shows just such a negative-then-positive pair of arrivals within the first 3 s. These were interpreted in previous work as a lowvelocity layer formed by a midcrustal magma body that is encountered by rays passing under the volcano. However, such a model does not explain the opposite polarity pair of arrivals (positive-then-negative) seen at the same delay time on azimuths pointing away from the volcano on the radial component (Fig. 2a), nor the large amplitude arrivals with polarity flips with the same timing on the transverse component (Fig. 2b). The combined out-of-plane arrivals on the radial and transverse components show an obvious pair with opposing polarity flips over backazimuth (Fig. 2e) with 360° periodicity. Applying the harmonic Fourier decomposition, the resulting  $A_1$  harmonic component (Fig. 2e, blue trace with red error bounds) shows pronounced peaks, one at 0.65 s corresponding to 6 km depth using the AVO velocity model for Akutan and one at 1.65 s or 10 km depth. The amplitude maximum points away from the volcanic center for the shallower arrival and toward the center for the deeper arrival.

The same pair of arrivals from upper and midcrustal depths is seen at all other stations, with the azimuths of the extrema and polarity nodes corresponding to each station's position relative to the volcanic center. Waveforms for all stations are shown in the supplemental material available in this article. Azimuthal results for all stations are shown in Figure 3. Arrival times are migrated to depth using the AVO velocity model for Akutan for consistency when comparing to AVO catalog seismicity (piercing points are shown in Fig. 4, and depths and positions of the upper and lower  $A_1$  arrivals at each station are also shown on cross sections in Fig. 5). The phase (azimuth of amplitude maximum; red arrows in Fig. 3) points

**Figure 3.** (a) Map of shallower  $A_1$  arrivals. Background shading is topography. White triangles are stations, and two-sided arrows show  $A_1$  polarity flip azimuths scaled by  $A_1$  amplitude and colored by depth; red one-sided arrows show the direction of phase (maximum amplitude of  $A_1$ ). (b) As in panel (a), but for the deeper  $A_1$  arrival. The color version of this figure is available only in the electronic edition.

away from the volcanic center for the shallower  $A_1$  arrival (Fig. 3a) and toward the center for the deeper one (Fig. 3b) at all stations except for the easternmost station that is farthest from the volcano. The azimuths perpendicular to the phase (azimuths where polarity flips occur; bars in Fig. 3) form a concentric pattern around the volcanic center for both arrivals at most stations. The pattern imaged by the  $A_1$  arrivals is thus one of dipping interfaces or foliation planes with dips that are concentric to the volcanic center (Schulte-Pelkum, Ross, *et al.*, 2020); details of the geometry are discussed subsequently.

Receiver function ray paths sample a cone that widens with depth beneath the station. Interfaces with a concentric geometry under the volcano can thus be sampled accurately in our station-by-station azimuthal analysis, provided that cones are confined to the side of the volcano where the station is situated. To test whether each station is sampling a footprint contained on the same side of the volcano within the average depth ranges of the observed  $A_1$  arrivals described in the following, we plot the ray piercing points for all receiver functions in Figure 4, produced by tracing rays through the AVO velocity model for Akutan (Dixon *et al.*, 2013). The map confirms that piercing points from each single station do not cross to the opposite flank of the volcano.

Ray paths and piercing points are based on an infinite frequency approximation. The real signal is bandlimited and therefore subjected to averaging over a Fresnel zone. The power spectra of our receiver functions peak at a period of 1.5 s. Using this dominant period and the AVO Akutan velocity

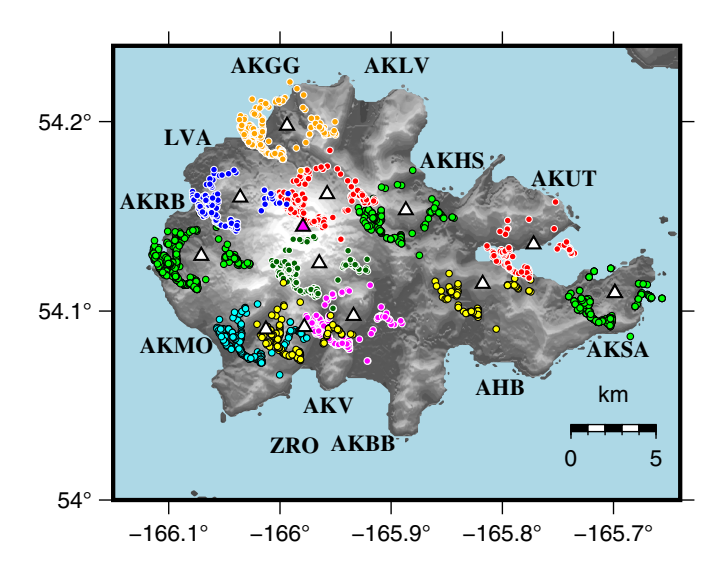


**Figure 4.** Map of topography (grayscale), stations (white triangles; station names shown), the center of the caldera (magenta triangle), and piercing points (dots colored by the center station for each set) for each receiver function at 12 km depth, the average for the deeper  $A_1$  arrival. The piercing points at 3 km depth (average depth of the shallower  $A_1$  arrival) cluster within 1 km of each station. The color version of this figure is available only in the electronic edition.

model, we calculate Fresnel zone widths (Zhu, 2002; Salmon et al., 2011) at the average depth of the shallower (3 km) and deeper  $A_1$  arrival (12 km). We obtain Fresnel zone widths of 3 km at 3 km depth and 7 km at 12 km depth. Cones consisting of these Fresnel zone widths centered on the ray piercing points should allow us to accurately sample a concentric geometry around the volcano (Fig. 4). Stations located close to the caldera (AKLV, AKV; Fig. 4) show shallower depths for both upper and lower interfaces (Fig. 5), which result in smaller Fresnel zones that are still confined to each side of the volcano.

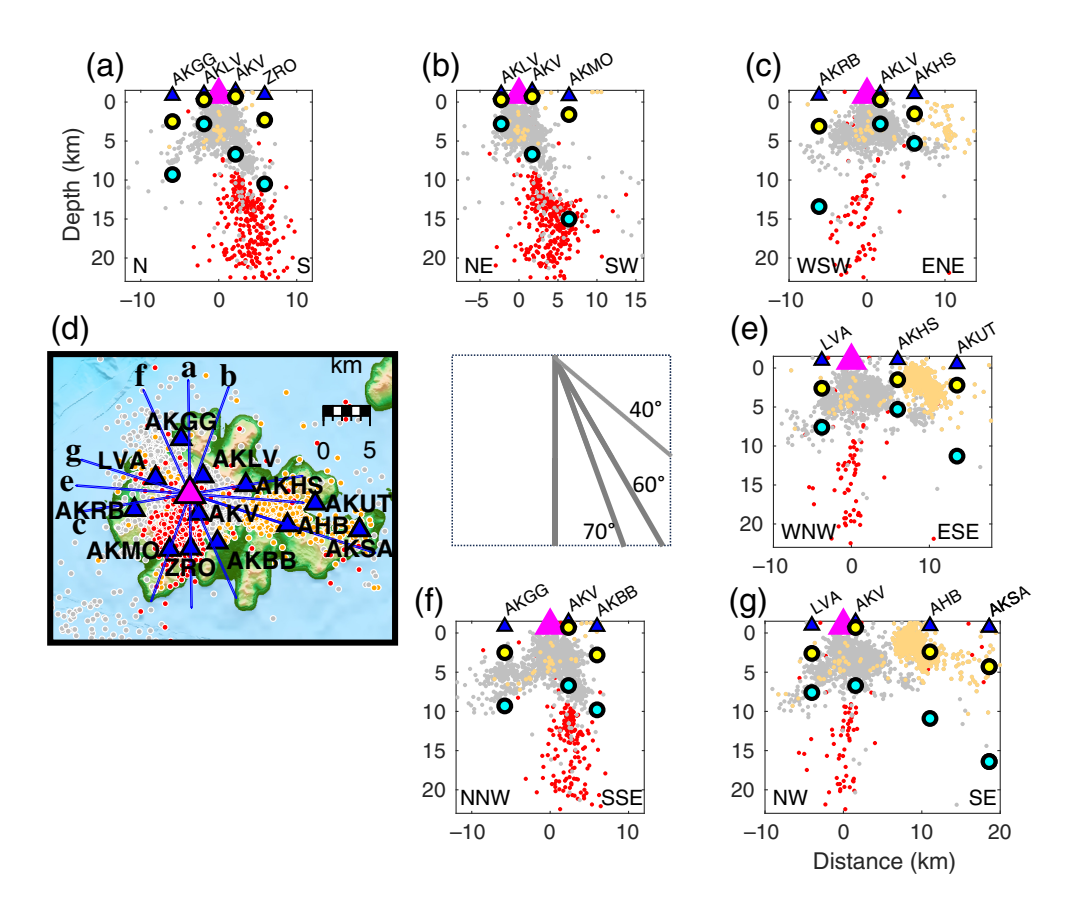
Figure 4 shows that piercing points and therefore Fresnel zones overlap between some neighboring stations. Rays with overlapping piercing points sample the same volume and should show similar arrival times if a converted phase is present at those azimuths and at the depth of ray overlap. However, the polarity and amplitude of a converted phase depend on the orientation of the ray relative to the dipping interface or dipping foliation at a contrast and are therefore expected to be different for an interface patch sampled by rays traveling in different directions. Comparisons of the depths of  $A_1$  arrivals in Figure 5, the timing of arrivals at azimuths of overlap from Figure 4, and waveform plots for each station (supplemental material) confirm that the imaged interface positions are consistent from station to station. As an example, station ZRO has piercing points to the east that overlap with piercing points seen toward the west at station AKBB near the depth of the lower  $A_1$  arrival (Fig. 4). The two  $A_1$  arrivals occur at nearly the same depth in the harmonic analysis (~10 km,

Fig. 5) and are seen at the same timing for ZRO-east and AKBB-west in station waveform plots (~1.7 s, supplemental material). Other station pairs show similarly consistent behavior for arrivals at overlapping piercing points from inspection of the same sets of figures.

There are two ways to generate a radial component receiver function arrival with a polarity flip in backazimuth. One is from a dipping interface between isotropic layers with a shear velocity contrast. Such an interface generates an azimuthally invariant  $R_0$ arrival with an amplitude proportional to the shear velocity contrast, independent of dip, superimposed on an azimuthally varying  $A_1$  arrival for which amplitude varies with interface dip. The latter can change polarity on the radial component as a function of backazimuth provided the interface dip is steep enough (Abe et al., 2011; Park and Levin, 2016; Feng et al., 2023). An important consideration for our interpretation is that a dipping contrast in velocity between isotropic layers is always accompanied by an  $R_0$  arrival on the radial component, with positive polarity if the velocity increases below the dipping interface and negative polarity if the velocity is decreased below the interface (Schulte-Pelkum and Mahan, 2014b). The transverse component only shows the  $A_1$  arrival in either case. For a slow-over-fast dipping interface in the isotropic case, the phase (amplitude maximum) points down-dip; for a fast-over-slow dipping interface (top of a low-velocity zone), the phase points up-dip (Schulte-Pelkum, Ross, et al., 2020).

The second option for generating a polarity flip on the radial component is from an interface with contrast in anisotropy in P velocity with a plunging symmetry axis. Unless such a contrast is accompanied by a contrast in isotropic shear velocity, there is no azimuthally invariant  $R_0$  component to the arrival. A horizontal symmetry axis on either side of the interface generates arrivals with polarity flips with 180° periodicity and relatively low amplitudes, whereas a plunging symmetry axis results in a dominant 360° periodicity signal with polarity reversals and higher amplitudes for the same contrast in anisotropy than in the horizontal axis case (Schulte-Pelkum and Mahan, 2014b; Park and Levin, 2016). These are seen on the radial and transverse components. In the simplest case of a hexagonal symmetry and assuming a slow symmetry axis (fast velocity planes), the phase points downdip for dipping fast planes for an interface above the stronger anisotropy and updip for an interface below the stronger anisotropy (Schulte-Pelkum, Ross, et al., 2020).

When interpreting the signals at Akutan, the first observation is that both arrivals at all stations increase in delay time as a function of station distance from the volcanic center (Figs. 3, 5). Therefore, both interfaces dip down outward from the volcanic center. Our interpretation thus has to explain an upper interface with an outward dip and  $A_1$  arrival phase pointing outward, and a lower interface with an outward dip and  $A_1$  phase pointing inward (Fig. 3). If one were to try to accomplish this using an isotropic model, the upper interface would have to have a slower-over-faster shear velocity contrast and the



**Figure 5.** Cross sections; panels are positioned roughly in line with profiles on the overview map (a) Depth cross-section with caldera center (magenta triangle), stations (blue triangles), upper (yellow circle), and lower (cyan circle)  $A_1$  arrival plotted under each station (actual footprint width as in Fig. 4), seismicity from AVO catalog (VT in gray, 1996 VT in orange, and LP in red). All depths are referenced to sea level and  $A_1$  arrival depths are corrected for station elevation. Stations and seismicity within 2 km of the profile line are displayed; profile azimuth is shown in panel (d). (b,c) Same as panel (a) but for other profiles shown in panel (d). (d) Map of topography, VT seismicity (gray dots), 1996 swarm VT seismicity (orange dots), LP seismicity (red dots), caldera center (magenta triangle), and stations (blue triangles with station name shown). Small letters designate profile ends shown on the left of panels (a–c) and (e–g). (e–g) Same as panels (a–c). All have no vertical exaggeration, dips are true angles; the center panel shows a visual guide to dip angles of 40°–70° in the depth profiles. The color version of this figure is available only in the electronic edition.

lower interface a faster-over-slower shear velocity contrast (Schulte-Pelkum and Mahan, 2014b). Such a model does fit the observations except for one important mismatch in  $R_0$ . The upper interface in such a model would show a positive  $R_0$  arrival and the lower interface a negative amplitude  $R_0$  arrival (Schulte-Pelkum and Mahan, 2014b). In the observed signal, both the upper and lower  $A_1$  arrivals show a concurrent positive amplitude  $R_0$  arrival (Fig. 2e). None of the stations show a prominent negative polarity  $R_0$  arrival at the same time as the second (lower)  $A_1$  arrival (supplemental material). We thus exclude a simple model of an isotropic high-velocity core underlain by a low-velocity isotropic magma-rich region (Janiszewski *et al.*, 2013; Syracuse *et al.*, 2015).

We next explore models with plunging axis anisotropy between the two dipping interfaces. The phase pointing outward for the upper arrival and inward for the lower (Fig. 3) dictates outward dipping fast planes if slow axis symmetry is assumed (Schulte-Pelkum, Ross, et al., 2020). Such symmetry can be explained by outward dipping dikes and/or cracks. If the anisotropy is dominated by crystallographically preferred orientation (CPO), outward dipping fast planes can be due to amphibole- and/or mica-dominated magmatic fabric (Frothingham et al., 2023). Another possibility in the CPOdominated case is inward plunging fast axis symmetry due to feldspar-dominated magmatic fabric (Frothingham et al., 2023).

The two prominent  $A_1$ arrivals are associated with small amplitude positive arrivals on the azimuthally invariant radial component  $(R_0)$ , consistent with small isotropic velocity increases downward at each interface bounding the anisotropic layer and inconsiswith a low-velocity layer below either interface. Anisotropy of 5%-10% is sufficient to generate the observed amplitudes (Brownlee et al., 2017). We discuss the likelihood of magmatic versus dike and/or crack fabric after a comparison with seismicity.

We evaluate the depths of the two  $A_1$  arrivals at each station and compare their locations and depths to that of seismicity in the AVO catalog (Power *et al.*, 2020). The AVO catalog shows event categories of volcanotectonic (VT) or long-period (LP) as classified by analysts, which broadly agree with the quantitative measures applied by Song *et al.* (2023). Figure 5 shows depth cross sections with VT and LP seismicity and  $A_1$  arrivals migrated using the same velocity model as that used for locating the seismicity (Dixon *et al.*, 2013) for internal consistency. We display profiles radial to the center of the caldera (center coordinates 54.14458° N, -165.97930° E) that include stations and seismicity located within 2 km of the profile.

Connecting the upper  $A_1$  picks (yellow dots in Fig. 5) from station to station results in outward dips of the interface ranging from gentle to 45°. Connecting the lower  $A_1$  picks from

station to station in the profiles results in dips ranging from 30° to 60°. For comparison, incidence angles of the converted S-wave cone using the slowness values of the receiver functions in the data set and the AVO Akutan velocity model range from 80° to 85° (measured relative to the horizontal to allow comparison with dips) at 3 km depth (average depth of the upper interface), with 90% of the receiver functions steeper than 82°. At 12 km depth (average of the lower interface), ray angles from the horizontal are 77°-83°, with 90% steeper than 79°. Because their dips are shallower than the ray angles, both interfaces are therefore intersected by the rays and corresponding Fresnel zones and should be captured appropriately by the harmonic analysis described earlier. The dip of the interfaces, particularly of the more steeply dipping lower interface, is also visible in the individual station plots (Fig. 2; supplemental material), where the lower  $A_1$  arrival shows moveout, with later arrivals in the "away" direction and earlier arrivals in the "toward" direction. The moveout is comparable to or less than the pulse width and width of the sliding window of 0.25 s used in the harmonic analysis, allowing the arrivals to be captured across all azimuths.

North–south-oriented profiles (Fig. 5a,b,f) show a cone of VT seismicity dipping away from the caldera center at angles of  $\sim$ 60°–70° from the horizontal. East–west-oriented profiles (Fig. 5c,e,g) show shallower dip angles, down to  $\sim$ 40° for the upper limit of the main VT seismicity cloud. Events from a VT swarm that occurred in 1996 are displayed in a different color and extend at shallower depths up to 20 km away from the center to the east. This swarm was previously interpreted as fault reactivation and dike intrusion into a preexisting fault with an orientation modulated by the regional arc stress field (Lu *et al.*, 2000; Tibaldi and Bonali, 2017). Nonconcentric  $A_1$  arrivals at the easternmost station AKUT (Figs. 3, 5) may be due to interactions with the regional stress field and east–west faulting on this side of the island (Stelling *et al.*, 2015).

The upper interface  $A_1$  arrivals similarly dip away from the center and separate the main volume of VT seismicity from a nearly aseismic volume above, except for the 1996 swarm. The lower limit of most of the VT seismicity also dips down away from the volcanic center. It largely coincides with the deeper  $A_1$  arrivals, which separate the VT volume from a deeper volume containing LP seismicity. The layer defined by the upper and lower  $A_1$  arrivals thickens and deepens away from the volcanic center.

## **Discussion**

Previous work on Akutan placed VT seismicity above an inferred magma reservoir and LP seismicity below it (Song et al., 2023). VT seismicity showed repeating events and a slight temporal preference (Song et al., 2023) for occurrence during inflation episodes taking place every 2–3 yr (Lu et al., 2000; Ji and Herring, 2011; DeGrandpre et al., 2017; Ji et al., 2017; Wang et al., 2018), resulting in an interpretation

as triggered brittle rupture on faults. Deep LPs were more strongly correlated with inflation events and were attributed to magma movement (Song et al., 2023). All seismicity relocation studies conducted for Akutan show the same conically outward dipping features in VT seismicity as in the AVO catalog used in this study (Syracuse et al., 2015; Koulakov et al., 2021; Song et al., 2023). Surface fault traces are mainly mapped east of the volcanic center, with a few traces mapped in the north and south (Stelling et al., 2015). The dominant orientation of the available surface fault traces is west-northwest to east-southeast, showing little resemblance to the  $A_1$  orientations at depth, except for the easternmost station that is farthest from the volcanic center where the regional stress field presumably controls subsurface geometry.

Tomographically imaged velocity anomalies vary between studies. Syracuse et al. (2015) found in their  $V_P$  image a lensshaped high-velocity ( $<10\% V_P$  anomaly) feature at depths of  $\sim$ 2–7 km centered under the caldera, with its upper boundary dipping down outward more steeply to the west and more gently to the east, similar to the dips of our interfaces from  $A_1$  arrivals showed on our east-west profiles c, e, and g in Figure 5. They also imaged a low- $V_P$  feature beneath it and offset to the east that they interpreted as a magma chamber, and interpreted outward dipping features in seismicity above the magma chamber and around the high-velocity lens as inflation and deflation cracking. Their  $V_S$  image is less detailed (likely due to sparser local S picks and broader sensitivity of surface waves in their joint inversion), with a mostly horizontal high-velocity anomaly from 2 to 5 km depth and no magma chamber signature. Both Syracuse et al. (2015) and Song et al. (2023) display east-west cross sections that show the upper boundary of seismicity as well as the  $V_P$  high-velocity body imaged by Syracuse et al. (2015) dipping outward at ~50° to the east, similar to our upper  $A_1$  interface in the same location. The local earthquake tomography and relocation study by Koulakov et al. (2021) found high-velocity  $V_P$  and  $V_S$  anomalies of up to 10% in the upper ~5 km under the caldera center, with most of their cross sections suggesting an outward-dipping geometry of the high-velocity body. They did not image a low-velocity feature matching the  $V_P$  inferred magma chamber from Syracuse et al. (2015), although most of their profiles show a weaker low-velocity feature at depths near 5 km and beneath their highest velocity anomalies.

The tomographic studies offer additional clues to separating the effects of anisotropy from those of dipping interfaces between isotropic layers at Akutan. Receiver functions are sensitive to isotropic  $V_S$  contrasts and anisotropic  $V_P$  contrasts (Park and Levin, 2016). We do not attempt to model the waveforms at each station in detail because of nonuniqueness, particularly when modeling anisotropy. For instance, even when assuming the highest anisotropic symmetry (hexagonal), one would have to vary not only the dip of the contrast in anisotropy, the plunge of the symmetry axis, and strength

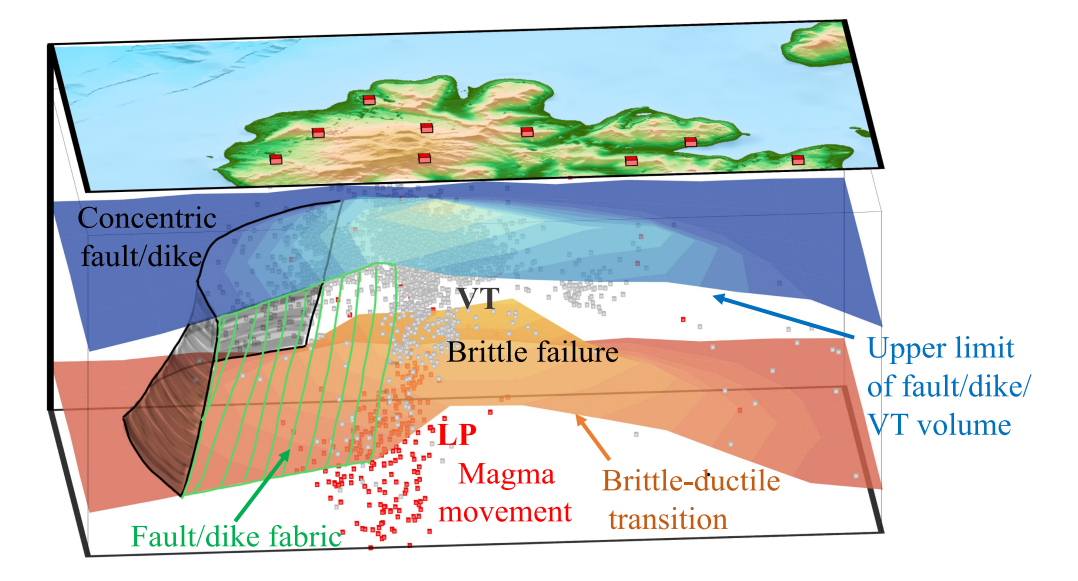


**Figure 6.** Conceptual schematic. The top layer is topography, stations in red. The vertical dimension is depth. All layers are cut away on an east–west line slightly south of the volcanic center. The view is from the south with an azimuth of 185° and elevation angle of 20°. The middle blue layer is a surface fitted to the shallower  $A_1$  arrivals. The bottom orange layer is a surface fitted to the deeper  $A_1$  arrivals, interpreted as the brittle–ductile transition based on the change from the main VT seismicity (gray cubes) volume to dominant LP (red cubes) seismicity. The gray shape represents part of a concentric ring fault or dike structure. Green lines represent a cutout face of the volume between the upper and lower surfaces that contains VT seismicity and anisotropic fabric with outward-dipping fast planes generating the  $A_1$  arrivals at the surfaces. Dimensions are not to scale. The color version of this figure is available only in the electronic edition.

of anisotropy, but also the off-axis hexagonal anisotropy parameter (the fifth parameter), which has a significant influence on waveform appearance (Schulte-Pelkum and Mahan, 2014a; Kawakatsu, 2016, 2018; Brownlee et al., 2017) and is not well constrained for volcanic environments. However, we can make broad quantitative estimates as follows.  $A_1$  amplitudes of the range observed here can be generated with <10% anisotropy (Brownlee et al., 2017). Modeling (Frederiksen and Bostock, 2000) shows that comparable  $A_1$  amplitudes generated with dipping interfaces between isotropic layers require  $V_S$  contrasts of ~40%. Imaged isotropic  $V_S$  anomalies (Syracuse et al., 2015; Koulakov et al., 2021) have a range of up to ~15%. Although tomographic studies tend to underestimate velocity anomaly amplitudes, checkerboard tests suggest that anomaly amplitudes should be recovered close to their original strength at least in parts of the tomographic volume (Koulakov et al., 2021), making it unlikely that dipping contrasts between purely isotropic layers with  $V_S$  variations large enough to generate the observed  $A_1$  amplitudes are present under every station in our analysis. This discrepancy combined with the lack of an azimuthally invariant negative arrival that would be required to generate the observed signals as discussed in the Results section leads us to conclude that anisotropy within the volume between the two interfaces with  $A_1$  conversions is required, and we assume the presence of anisotropy in the volume between the two  $A_1$  interfaces in the rest of our discussion. The possible effect of anisotropy in the tomographic studies conducted to date, which assumed purely isotropic models, has yet to be quantified.

Our main findings are constraints on the physical characteristics of the conical VT seismicity volume. The upper and lower boundaries of the conical volume with anisotropy as imaged by receiver functions  $(A_1 \text{ arrivals})$  coincide with the boundaries of the VT seismicity volume at most stations (Fig. 5). Dips of these conical boundaries are similar to the gentle to intermediate dips inferred from tomography and seismicity in previous work (Syracuse et al., 2015; Koulakov et al., 2021; Song et al., 2023) on east-west profiles and steeper (up to ~70°) dips on northsouth profiles. We interpret the

lower boundary of the volume with VT seismicity and anisotropy as the brittle–ductile transition, deepening away from the volcanic center (Fig. 6) as discussed in the context of magmatic systems by White and McCausland (2019). Steep outward dips of modeled oblate spheroids to match inflation episodes (DeGrandpre *et al.*, 2017) may match such an outward-dipping geometry.

We interpret the anisotropy with outward-dipping conical fast planes inferred within the VT seismicity volume as follows (Fig. 6). Because of the prevalence of seismicity in the volume and the similarity between outward-dipping patterns in seismicity and the outward dips required by fast-plane anisotropy, we consider crack and dike fabric to be more likely than purely CPO-dominated magmatic fabric. The latter forms under rigid body rotation of crystals in the presence of melt (Frothingham *et al.*, 2023), which seems less likely in our case given the lack of a low-velocity signature of the volume.

We next explore how an outward-dipping fault and dike fabric could form. Ring faulting occurs under calderas, and microseismicity with outward dips has been interpreted as outlining ring faults (Mori and McKee, 1987; Syracuse *et al.*, 2015). Although analog and numerical modeling experiments suggest vertical or near-vertical in- or outward-dipping ring faults (Geyer and Marti, 2014), smaller calderas can favor outward dips (Folch and Marti, 2004), and teleseismic

observations of vertical compensated linear vector dipole moment tensors from moderate magnitude earthquakes under volcanoes suggest shallower dip angles of ring faults of ~50° to 70° (Shuler *et al.*, 2013), similar to the angles formed by the VT seismicity in our observations (Fig. 5). Ring faults can capture dikes (Walter, 2008; Browning and Gudmundsson, 2015), interact with rheological layering in the medium they form in (Kinvig *et al.*, 2009; Li, 2022), and affect estimates of intrusion volumes based on ground deformation (Liu *et al.*, 2019). Caldera structures can be nested (Lai *et al.*, 2021).

We propose that the volume containing the main VT seismicity hosts a pervasive fabric with outward-dipping concentric fast planes formed by ring faults and dikes that are also concentric and parallel to the fast planes (Fig. 6). The upper and lower limits of this fabric give rise to the concentric pattern seen in the upper and lower  $A_1$  arrivals (Fig. 3). Growth of ring faults and concentric dikes is driven by magma transport and inflation and deflation beneath the brittle-ductile transition in the zone hosting LP seismicity. The resulting fabric in turn focuses microseismicity occurring as a response to this deeper deformation (Syracuse et al., 2015; Song et al., 2023). Interaction with the regional stress field (Johnson et al., 2010; Tibaldi and Bonali, 2017) results in shallower dips of the volume boundary and a wider zone of VT seismicity and anisotropic fabric in the eastwest (along-arc) orientation and steeper dips in the north-south or arc-perpendicular orientation.

Our proposed outward-dipping anisotropic geometry provides an interesting context to recent work using surface waves to image radial anisotropy under volcanoes, such as Okmok in the Aleutians (Miller et al., 2020) and in the Cascade volcanoes inland from the North American western subduction boundary (Jiang et al., 2023). In both cases, results suggest horizontal fast planes under volcanic centers, surrounded by areas with vertical fast planes. They were interpreted as central (horizontal) sill complexes with surrounding ring-shaped (vertical) dike complexes (Miller et al., 2020). However, the assumption of radial anisotropy (vertical symmetry axis) only allows resolving vertical or horizontal fast planes, and if the true geometry is one with dipping fast planes, they would likely be apparent as sills for shallow dips and as dikes for steep dips. In a concentric arrangement of outward-dipping dikes, the center may appear to have positive radial anisotropy (sills) and the surrounding ring may be resolved as vertical dikes by surface-wave radial anisotropy. Okmok shows concentric patterns in receiver function  $A_1$  arrivals (Schulte-Pelkum, Caine, et al., 2020) similar to those shown here for Akutan, leaving open the possibility that the radial anisotropy geometry obtained by Miller et al. (2020) may be underlain by concentric dipping fast planes. Recent method advances that invert for plunging axis anisotropic geometry on a lithospheric scale (Xie et al., 2017; Liu and Ritzwoller, 2024) may thus be interesting to apply to the crust under volcanoes. Many volcanoes along the Alaskan and Aleutian arcs show hints of concentric  $A_1$  patterns (SchultePelkum, Caine, et al., 2020), leaving open the possibility that the geometry discussed here is a common phenomenon.

## **Conclusions**

We have shown that receiver function arrivals with strong variations in amplitude and polarity as a function of backazimuth at Akutan volcano indicate an upper crustal and a midcrustal interface with contrasts in plunging axis anisotropy. Each interface shows a weak to no isotropic velocity increase with depth. The interfaces bracket the majority of VT seismicity from the AVO catalog, and most of the LP seismicity is located below the deeper interface. The anisotropy within the volume matches a model for which an upper to midcrustal fabric with concentric outward-dipping fast planes (concentric outwarddipping faults and dikes) localizes brittle VT seismicity in response to magma movement below. The midcrustal interface is interpreted as the brittle-ductile transition. Our imaging method allows mapping of the volume with concentric fabric away from present-day seismicity and thus provides a more geographically complete and independent constraint for the magmatic system on Akutan.

## **Data and Resources**

Waveform data used are from the seismic networks AV (Alaska Volcano Observatory [AVO]/U.S. Geological Survey [USGS]; doi: 10.7914/SN/ AV; Dixon et al., 2013) and AT (National Tsunami Warning Center Alaska Seismic Network; doi: 10.7914/SN/AT; National Oceanic and Atmospheric Administration [NOAA], 1967). Data access and preprocessing were performed using Standing Order for Data (SOD, available at http://www.seis.sc.edu/sod; Owens et al., 2004). The AVO seismicity catalog is available at https://pubs.usgs.gov/publication/sir20195037 for years 1989-2018 and https://earthquake.usgs.gov/earthquakes/search for 2019-present. Maps were made using Generic Mapping Tools (GMT; Wessel et al., 2019). The Raysum code (Frederiksen and Bostock, 2000) was used for forward modeling and is available at ~https:// home.cc.umanitoba.ca/~frederik/Software/. AVO information is available at avo.alaska.edu/volcanoes. All websites were last accessed in March 2024. The supplemental material of this article is available online and consists of waveform plots as in Figure 2 for all stations as well as tables with the  $A_1$  solutions.

# **Declaration of Competing Interests**

The authors acknowledge that there are no conflicts of interest recorded.

# Acknowledgments

This research was supported by National Science Foundation (NSF) Grant Numbers EAR-2051243 and EAR-1735890. The authors thank John Power, Helen Janiszewski, Wes Thelen, William Shinevar, Will Yeck, David Shelly, and Jeff Benowitz for the discussions. Comments by two anonymous reviewers and Phil Dawson helped improve the article significantly. The facilities of the EarthScope Consortium were used for access to waveforms and related metadata used in this study; these services are funded through the Seismological Facility for the

Advancement of Geoscience (SAGE) Award of the NSF under Cooperative Agreement Number EAR-1724509. Any use of trade, firm, or product names is for descriptive purposes only and does not imply endorsement by the U.S. Government.

#### References

- Abe, Y., T. Ohkura, K. Hirahara, and T. Shibutani (2011). Common-conversion-point stacking of receiver functions for estimating the geometry of dipping interfaces, *Geophys. J. Int.* **185**, no. 3, 1305–1311, doi: 10.1111/j.1365-246X.2011.05001.x.
- Browning, J., and A. Gudmundsson (2015). Caldera faults capture and deflect inclined sheets: An alternative mechanism of ring dike formation, *Bull. Volcanol.* 77, no. 1, doi: 10.1007/s00445-014-0889-4.
- Brownlee, S. J., V. Schulte-Pelkum, A. Raju, K. Mahan, C. Condit, and O. F. Orlandini (2017). Characteristics of deep crustal seismic anisotropy from a compilation of rock elasticity tensors and their expression in receiver functions, *Tectonics* 36, no. 9, 1835–1857, doi: 10.1002/2017TC004625.
- Buurman, H., C. J. Nye, M. E. West, and C. Cameron (2014). Regional controls on volcano seismicity along the Aleutian arc, *Geochem. Geophys. Geosys.* **15**, no. 4, 1147–1163, doi: 10.1002/2013GC005101.
- Cashman, K. V., R. S. J. Sparks, and J. D. Blundy (2017). Vertically extensive and unstable magmatic systems: A unified view of igneous processes, *Science* **355**, no. 6331, doi: 10.1126/science.aag3055.
- DeGrandpre, K., T. Wang, Z. Lu, and J. T. Freymueller (2017). Episodic inflation and complex surface deformation of Akutan volcano, Alaska revealed from GPS time-series, *J. Volcanol. Geotherm. Res.* 347, 337–359, doi: 10.1016/j.jvolgeores.2017.10.003.
- Dixon, J., S. Stihler, J. Power, M. Haney, T. Parker, C. Searcy, and S. Prejean (2013). Catalog of earthquake hypocenters at Alaskan volcanoes: January 1 through December 31, 2012, U.S. Geol. Surv. Data Series 789, available at https://pubs.usgs.gov/ds/789/ (last accessed March 2024).
- Ewert, J., A. Diefenbach, and D. Ramsey (2018). 2018 update to the U.S. Geological Survey national volcanic threat assessment, U.S. Geol. Surv. Sci. Investig. Rept. 2018-51/0, doi: 10.3133/sir20185140.
- Feng, M., L. Chen, S. Wei, X. Wang, X. Wang, and Z. Wu (2023). A new method to estimate slab dip direction using receiver functions and its application in revealing slab geometry and a diffuse plate boundary beneath Sumatra, *J. Geophys. Res.* 128, no. 4, doi: 10.1029/2022JB024598.
- Folch, A., and J. Marti (2004). Geometrical and mechanical constraints on the formation of ring-fault calderas, *Earth Planet. Sci. Lett.* **221,** nos. 1/4, 215225, doi: 10.1016/S0012-821X(04)00101-3.
- Frederiksen, A., and M. Bostock (2000). Modelling teleseismic waves in dipping anisotropic structures, *Geophys. J. Int.* **141,** 401–412, doi: 10.1046/j.1365-246x.2000.00090.x.
- Frothingham, M. G., K. H. Mahan, V. Schulte-Pelkum, P. Goncalves, and M. Zucali (2023). Confronting solid-state shear bias: Magmatic fabric contribution to crustal seismic anisotropy, *Geophys. Res. Lett.* **50**, no. 6, doi: 10.1029/2022GL102399.
- Geyer, A., and J. Marti (2014). A short review of our current understanding of the development of ring faults during collapse caldera formation, *Front. Earth Sci.* 2, doi: 10.3389/feart.2014.00022.
- Janiszewski, H. A., G. A. Abers, D. J. Shillington, and J. A. Calkins (2013). Crustal structure along the Aleutian island arc: New insights from receiver functions constrained by active-source

- data, Geochem. Geophys. Geosys. 14, 2977–2992, doi: 10.1002/ggge.20211.
- Janiszewski, H. A., L. S. Wagner, and D. C. Roman (2020). Aseismic mid-crustal magma reservoir at Cleveland Volcano imaged through novel receiver function analyses, *Sci. Rep.* 10, no. 1, doi: 10.1038/s41598-020-58589-0.
- Ji, K. H., and T. A. Herring (2011). Transient signal detection using GPS measurements: Transient inflation at Akutan volcano, Alaska, during early 2008, *Geophys. Res. Lett.* 38, doi: 10.1029/2011GL046904.
- Ji, K. H., S.-H. Yun, and H. Rim (2017). Episodic inflation events at Akutan Volcano, Alaska, during 2005-2017, Geophys. Res. Lett. 44, no. 16, 8268-8275, doi: 10.1002/2017GL074626.
- Jiang, C., B. Schmandt, G. A. Abers, E. Kiser, and M. S. Miller (2023). Segmentation and radial anisotropy of the deep crustal magmatic system beneath the Cascades arc, *Geochem. Geophys. Geosys.* 24, no. 3, doi: 10.1029/2022GC010738.
- Johnson, J. H., S. Prejean, M. K. Savage, and J. Townend (2010). Anisotropy, repeating earthquakes, and seismicity associated with the 2008 eruption of Okmok volcano, Alaska, *J. Geophys. Res.* 115, doi: 10.1029/2009JB006991.
- Kawakatsu, H. (2016). A new fifth parameter for transverse isotropy, *Geophys. J. Int.* **204**, 682–685, doi: 10.1093/gji/ggv479.
- Kawakatsu, H. (2018). A new fifth parameter for transverse isotropy III: Reflection and transmission coefficients, *Geophys. J. Int.* 213, no. 1, 426433, doi: 10.1093/gji/ggy003.
- Kinvig, H. S., A. Geyer, and J. Gottsmann (2009). On the effect of crustal layering on ring-fault initiation and the formation of collapse calderas, *J. Volcanol. Geotherm. Res.* 186, nos. 3/4, 293–304, doi: 10.1016/j.jvolgeores.2009.07.007.
- Koulakov, I., V. Komzeleva, S. Z. Smirnov, and S. B. Bortnikova (2021). Magma-fluid interactions beneath Akutan volcano in the Aleutian arc based on the results of local earthquake tomography, J. Geophys. Res. 126, no. 3, doi: 10.1029/2020JB021192.
- Lai, V. H., Z. Zhan, Q. Brissaud, O. Sandanbata, and M. S. Miller (2021). Inflation and asymmetric collapse at Kilauea summit during the 2018 eruption from seismic and infrasound analyses, J. Geophys. Res. 126, no. 10, doi: 10.1029/2021JB022139.
- Li, Y. (2022). Syn-eruptive normal faults in tephra rings and formation mechanisms, *J. Struct. Geol.* **161**, 104,685.
- Ligorría, J., and C. Ammon (1999). Iterative deconvolution and receiver-function estimation, *Bull. Seismol. Soc. Am.* **89**, no. 5, 1395–1400.
- Liu, C., and M. Ritzwoller (2024). Seismic anisotropy and deep crustal deformation across Alaska, *J. Geophys. Res.* **129**, doi: 10.1029/2023[B028525.
- Liu, Y.-K., J. Ruch, H. Vasyura-Bathke, and S. Jonsson (2019). Influence of ring faulting in localizing surface deformation at subsiding calderas, *Earth Planet. Sci. Lett.* **526**, doi: 10.1016/j.epsl.2019. 115784.
- Lu, Z., C. Wicks, J. Power, and D. Dzurisin (2000). Ground deformation associated with the March 1996 earthquake swarm at Akutan volcano, Alaska, revealed by satellite radar interferometry, *J. Geophys. Res.* **105**, no. B9, 21,483–21,495, doi: 10.1029/2000JB900200.
- Miller, D., N. Bennington, M. Haney, P. Bedrosian, K. Key, C. Thurber, L. Hart, and S. Ohlendorf (2020). Linking magma storage and ascent to eruption volume and composition at an arc caldera, *Geophys. Res. Lett.* 47, no. 14, doi: 10.1029/2020GL088122.

- Mori, J., and C. McKee (1987). Outward-dipping ring-fault structure at Rabaul caldera as shown by earthquake locations, *Science* **235**, no. 4785, 193–195, doi: 10.1126/science.235.4785.193.
- National Oceanic and Atmospheric Administration (NOAA) (1967). National Oceanic and Atmospheric Administration (USA), National Tsunami Warning Center Alaska Seismic Network [Data set], *International Federation of Digital Seismograph Networks*, doi: 10.7914/SN/AT.
- Owens, T., H. Crotwell, C. Groves, and P. Oliver-Paul (2004). Sod: Standing order for data, *Seismol. Res. Lett.* **75**, no. 4, 515–520.
- Park, J., and V. Levin (2016). Anisotropic shear zones revealed by backazimuthal harmonics of teleseismic receiver functions, *Geophys. J. Int.* 207, no. 2, 1216–1243, doi: 10.1093/gji/ggw323.
- Portner, D. E., L. S. Wagner, H. A. Janiszewski, D. C. Roman, and J. A. Power (2020). Ps-P tomography of a midcrustal magma reservoir beneath Cleveland Volcano, Alaska, *Geophys. Res. Lett.* 47, no. 22, doi: 10.1029/2020GL090406.
- Power, J. A., M. M. Haney, S. M. Botnick, J. P. Dixon, D. Fee, A. M. Kaufman, D. M. Ketner, J. J. Lyons, T. Parker, J. F. Paskievitch, et al. (2020). Goals and development of the Alaska Volcano Observatory seismic network and application to forecasting and detecting volcanic eruptions, Seismol. Res. Lett. 91, no. 2A, 647–659, doi: 10.1785/0220190216.
- Salmon, M. L., T. A. Stern, and M. K. Savage (2011). A major step in the continental Moho and its geodynamic consequences: The Taranaki-Ruapehu line, New Zealand, *Geophys. J. Int.* **186**, no. 1, 32–44, doi: 10.1111/j.1365-246X.2011.05035.x.
- Savage, M. (1998). Lower crustal anisotropy or dipping boundaries? Effects on receiver functions and a case study in New Zealand, J. Geophys. Res. 103, no. B7, 15,069–15,087, doi: 10.1029/98JB00795.
- Schulte-Pelkum, V., and K. H. Mahan (2014a). Imaging faults and shear zones using receiver functions, *Pure Appl. Geophys.* **171,** no. 11, 2967–2991, doi: 10.1007/s00024-014-0853-4.
- Schulte-Pelkum, V., and K. H. Mahan (2014b). A method for mapping crustal deformation and anisotropy with receiver functions and first results from USArray, *Earth Planet. Sci. Lett.* **402**, 221–233, doi: 10.1016/j.epsl.2014.01.050.
- Schulte-Pelkum, V., J. S. Caine, J. V. Jones III, and T. W. Becker (2020). Imaging the tectonic grain of the Northern Cordillera orogen using Transportable Array receiver functions, *Seismol. Res. Lett.* **91**, no. 6, 3086–3105, doi: 10.1785/0220200182.
- Schulte-Pelkum, V., Z. E. Ross, K. Mueller, and Y. Ben-Zion (2020). Tectonic inheritance with dipping faults and deformation fabric in the brittle and ductile southern California crust, *J. Geophys. Res.* **125**, no. 8, doi: 10.1029/2020JB019525.
- Shillington, D., H. Van Avendonk, W. Holbrook, P. Kelemen, and M. Hornbach (2004). Composition and structure of the central Aleutian island arc from arc-parallel wide-angle seismic data, *Geochem. Geophys. Geosys.* 5, doi: 10.1029/2004GC000715.

- Shuler, A., G. Ekstroem, and M. Nettles (2013). Physical mechanisms for vertical-CLVD earthquakes at active volcanoes, *J. Geophys. Res.* **118**, no. 4, 1569–1586, doi: 10.1002/jgrb.50131.
- Song, Z., Y. J. Tan, and D. C. Roman (2023). Deep long-period earth-quakes at Akutan volcano from 2005 to 2017 better track magma influxes compared to volcano-tectonic earthquakes, *Geophys. Res. Lett.* **50**, no. 10, doi: 10.1029/2022GL101987.
- Stelling, P., N. H. Hinz, A. Kolker, and M. Ohren (2015). Exploration of the Hot Springs Bay Valley (HSBV) geothermal resource area, Akutan, Alaska, *Geothermics* 57, 127–144, doi: 10.1016/j.geothermics.2015.05.002.
- Syracuse, E. M., M. Maceira, H. Zhang, and C. H. Thurber (2015). Seismicity and structure of Akutan and Makushin Volcanoes, Alaska, using joint body and surface wave tomography, *J. Geophys. Res.* **120**, no. 2, 1036–1052, doi: 10.1002/2014JB011616.
- Tibaldi, A., and F. L. Bonali (2017). Intra-arc and back-arc volcano-tectonics: Magma pathways at Holocene Alaska-Aleutian volcanoes, *Earth Sci. Rev.* **167**, 1–26, doi: 10.1016/j.earscirev.2017.02.004.
- Walter, T. R. (2008). Facilitating dike intrusions into ring-faults, in *Caldera volcanism: Analysis, Modelling and Response*, J. Gottsmann and J. Marti (Editors), Vol. 10, Elsevier Science, Amsterdam, The Netherlands, 35–74, doi: 10.1016/S1871-644X(07)00009-5.
- Wang, T., K. DeGrandpre, Z. Lu, and J. T. Freymueller (2018). Complex surface deformation of Akutan volcano, Alaska revealed from InSAR time series, *Int. J. Appl. Earth Obs. Geoinf.* 64, 171– 180, doi: 10.1016/j.jag.2017.09.001.
- Waythomas, C. (1999). Stratigraphic framework of Holocene volcaniclastic deposits, Akutan Volcano, east-central Aleutian Islands, Alaska, *Bull. Volcanol.* **61**, no. 3, 141–161, doi: 10.1007/s004450050268.
- Wessel, P., J. F. Luis, L. Uieda, R. Scharroo, F. Wobbe, W. H. F. Smith, and D. Tian (2019). The Generic Mapping Tools Version 6, Geochem. Geophys. Geosys. 20, no. 11, 5556–5564, doi: 10.1029/2019GC008515.
- White, R. A., and W. A. McCausland (2019). A process-based model of pre-eruption seismicity patterns and its use for eruption forecasting at dormant stratovolcanoes, *J. Volcanol. Geotherm. Res.* **382**, no. SI, 267–297, doi: 10.1016/j.jvolgeores.2019.03.004.
- Xie, J., M. H. Ritzwoller, W. Shen, and W. Wang (2017). Crustal anisotropy across eastern Tibet and surroundings modeled as a depth-dependent tilted hexagonally symmetric medium, *Geophys. J. Int.* 209, no. 1, 466–491, doi: 10.1093/gji/ggx004.
- Zhu, L. (2002). Deformation in the lower crust and downward extent of the San Andreas Fault as revealed by teleseismic waveforms, *Earth Planets Space* **54**, no. 11, 1005–1010, doi: 10.1186/BF03353293.

Manuscript received 25 March 2024 Published online 27 June 2024